

Effects of organized mesoscale heating on the MJO and precipitation in E3SMv1

Chih-Chieh Chen¹, Jadwiga H. Richter², Changhai Liu², Mitchell W Moncrieff², Qi Tang³, Wuyin Lin⁴, Shaocheng Xie⁵, and Philip J. Rasch⁶

¹NCAR CGD

²National Center for Atmospheric Research (UCAR)

³Lawrence Livermore National Laboratory (DOE)

⁴Brookhaven National Laboratory (DOE)

⁵Lawrence Livermore National Laboratory

⁶Pacific Northwest National Laboratory (DOE)

November 24, 2022

Abstract

Mesoscale organization of convection is typically not represented in global circulation models, and hence its influence on the global circulation is not accounted for. A parameterization aiming at representing the dynamical and physical effects of the circulation associated with organized convection, referred to as the multiscale coherent structure parameterization (MCSP), is implemented in the Energy Exascale Earth System Model version 1 (E3SMv1). Simulations are conducted to assess its impact on the simulated climate. Besides E3SMv1 simulations, we performed high-resolution (1 km) simulations using the Weather Research and Forecasting (WRF) Model to determine the temperature tendencies induced by mesoscale convective systems embedded in deep convection. We tuned the free parameters of the MCSP based on the WRF simulations. We found that the MCSP enhances Kelvin wave spectra in E3SMv1, improves the representation of the Madden-Julian Oscillation, and reduces model precipitation biases over the tropical Pacific.

35 **Abstract**

36

37 Mesoscale organization of convection is typically not represented in global circulation models,
38 and hence its influence on the global circulation is not accounted for. A parameterization aiming at
39 representing the dynamical and physical effects of the circulation associated with organized convection,
40 referred to as the multiscale coherent structure parameterization (MCSP), is implemented in the Energy
41 Exascale Earth System Model version 1 (E3SMv1). Simulations are conducted to assess its impact on the
42 simulated climate. Besides E3SMv1 simulations, we performed high-resolution (1 km) simulations using
43 the Weather Research and Forecasting (WRF) Model to determine the temperature tendencies induced by
44 mesoscale convective systems embedded in deep convection. We tuned the free parameters of the MCSP
45 based on the WRF simulations. We found that the MCSP enhances Kelvin wave spectra in E3SMv1,
46 improves the representation of the Madden-Julian Oscillation, and reduces model precipitation biases
47 over the tropical Pacific.

48

49 **1 Introduction**

50 The transport and mixing of heat and momentum throughout the atmosphere largely control the
51 global circulation, and hence moisture and precipitation patterns. However, several transport processes
52 occur on scales much smaller than a global circulation model (GCM) grid box, and hence have to be
53 parameterized. Improvements in the representation of subgrid heat and momentum transport can lead to
54 significant model improvements in the representation of wind stresses, moisture and precipitation
55 patterns, and organized modes of variability [Richter and Rasch 2008]. In particular, convection is a large
56 source of heat and momentum transport in the atmosphere, both on scales of individual convective
57 plumes, as well as on scales of the order of 10-1000 km (mesoscales) [Moncrieff 1995, Houze 2004].

58

59 The importance of convective organization on the global circulation has been recognized for
60 more than three decades but parameterizations of the attendant processes are missing from GCMs.
61 Contemporary convective parameterizations commonly use a convective plume model (or a spectrum of
62 plumes) [Arakawa and Schubert 1974, Kain et al. 1990, D’Andrea et al. 2014, Chen and Mapes 2018].
63 This is appropriate for unorganized convection. However, the assumption of a gap between the cumulus
64 scale and the large-scale motion that underpins contemporary convective parameterizations fails to
65 recognize mesoscale dynamics manifested in squall lines, mesoscale convective systems (MCS),
66 mesoscale convective complexes (MCC), and multi-scale cloud systems associated with the Madden-
67 Julian Oscillation (MJO). Over 50% of convective precipitation in the tropics is provided by MCS

68 defined as heavily precipitating closely coupled cumulus ensembles embedded in the more moderately
69 precipitating stratiform regions of these systems [Nesbitt et al. 2006, Tao and Moncrieff 2009].

70
71 Mesoscale convective organization significantly modulates the life-cycle of moist convection, the
72 transport of heat, moisture, momentum and chemical constituents [Houze 2004, Houze 2014]. Organized
73 convection is abundant in environments featuring vertical wind shear and is typically associated with
74 counter-gradient momentum transport [Moncrieff 1992]. Moncrieff and Liu [2006] designed a hybrid
75 “predictor-corrector” framework to parameterize mesoscale convective systems and tested this approach
76 in the Weather Research and Forecasting (WRF) model with a 60 km grid over the United States
77 continent in summertime meteorological conditions. Specifically, a cumulus parameterization scheme
78 gives the convective heating profile (predictor) which is then adjusted by adding sine-like upper-
79 tropospheric warming and low-tropospheric cooling (i.e. 2nd baroclinic normal mode) heating corrector
80 that emulates the mesoscale heating profile associated with MCSs. Moncrieff, Liu and Bogenschutz
81 [2017] (hereafter MLB17) recently implemented a similar approach using the Community Atmosphere
82 MOdel (CAM) in the form of multiscale coherent structure parameterization (MCSP) where organized
83 convection is treated as coherent structures in a turbulent environment. MCSP is approximated by a
84 slantwise layer overturning dynamical model that exchanges tropospheric layers via convectively
85 generated mesoscale circulations (Fig. 1). Because slantwise layer overturning is not represented by
86 existing convective parameterizations in a GCM, it is thus appropriate to simply add the “missing”
87 mesoscale tendencies to traditional convective parameterizations. It follows that, for the first time, the
88 difference between GCM simulations with and without MCSP can directly measure the large-scale effects
89 of convective organization.

90
91 The implementation of MCSP was shown in MLB17 to improve precipitation biases in CAM
92 version 5.5 (CAM5.5), e.g., in the tropical west Pacific (TWP), equatorial Africa, and the Inter Tropical
93 Convergence Zone (ITCZ). MCSP also increased the Kelvin wave amplitude and extended the MJO
94 signal from zonal wavenumber 1 to a more realistic wavenumber 1 - 5 range (MLB17).

95
96 The Energy Exascale Earth System Model, version 1 (E3SMv1) is a new Earth system model
97 designed to meet the science needs of the nation and the mission of the Department of Energy (DOE).
98 E3SM currently does not represent heat or momentum transport associated with mesoscale convective
99 organization, so implementation of the MCSP introduces missing physical processes and can potentially
100 reduce E3SM’s biases, in particular, over the ITCZ, south Pacific convergence zone, and the maritime
101 continent. Parameterization of mesoscale momentum transport is needed for horizontal resolutions of 25

102 km or coarser, which are the resolutions to be used by next generations of E3SM for its low-resolution
 103 science applications.

104

105 **2 Mesoscale Heating Parameterization**

106 To account for the impact of multiscale convective systems, their induced heating is added to the
 107 existing deep convection parameterization. Following Moncrieff and Liu [2006] and Moncrieff et al.
 108 [2017], mesoscale heating in the stratiform region is represented simply as a 2nd baroclinic normal mode
 109 with amplitude proportional to the vertically averaged convective heating provided by the convective
 110 parameterization. While a realistic vertical distribution of mesoscale heating is considerably more
 111 complex [Moncrieff 1992], this simplification captures its dominant features.

112

113 Figure 2b illustrates the vertical profile of mesoscale heating, which is dominated by heating (H)
 114 in the trailing stratiform region and evaporative cooling (C) beneath. In the Moncrieff and Liu (2006)
 115 prototype, the simplest possible vertical profile of mesoscale heating in Fig. 2, is given by the following
 116 equations:

$$117 \quad Q(\sigma, z) = -\alpha Q_c(\sigma) \exp\left[2\alpha \frac{(z - z^*)}{(z_t - z_b)}\right] \quad (1)$$

$$118 \quad z^* = \frac{z_b + z_t - z_c}{2} \quad (2)$$

$$119 \quad Q_c(\sigma) = \frac{I}{(z_t - z_b)} \int_{z_b}^{\sigma} Q(\sigma) dz \quad (3)$$

120 where α is positive and is a free (tunable) parameter; z_b and z_t are the bottom and top of the convection
 121 respectively; z^* is the location where the heating profile crosses the zero line; Q_c is the average heating
 122 rate from the deep convection scheme.

123 **3 WRF Simulations**

124 We utilize version 4.0.3 of Weather and Research Forecasting model [Skamarock et al. 2008]
 125 (hereafter WRF) to carry out convection resolving simulations that will help to guide the free parameters
 126 in the mesoscale heating parameterization. WRF is a fully compressible, nonhydrostatic model with a
 127 terrain-following mass coordinate, suitable for use in a broad spectrum of applications across scales
 128 ranging from meters to thousands of kilometers. The computational domain is 4600 km x 1700 km at 2
 129 km grid spacing with 65 stretched vertical levels and model top at 25 hPa. The employed subgrid

130 parameterizations included the WRF single-moment 6-class microphysics [Hong and Lim 2006], the YSU
131 planetary boundary layer parameterization [Hong et al. 2006], the Noah-MP land surface model [Niu et
132 al. 2011], and the Rapid Radiative Transfer Model (RRTMG) for longwave and shortwave atmospheric
133 radiative fluxes [Iacono et al. 2008]. Spectral nudging was applied to wind and water vapor fields above
134 the planetary boundary layer to preserve the characteristics of large-scale circulation, while allowing the
135 development of sub-synoptic, mesoscale and convective processes. Two multi-day episodes of active
136 convection associated with an MJO event (MLB17) were selected for experimentation, corresponding to a
137 9-day convective period in the Indian Ocean (Fig. 3a) and a 14-day convective period in the western
138 Pacific (Fig. 4a), respectively. The hourly, 31-km-resolution ERA5 reanalysis data provided initial and
139 boundary conditions. It is seen from Figs. 3b and 4b that the observed convective systems are well
140 captured in the WRF convection resolving simulations in both the Indian Ocean and the western Pacific.
141 Therefore, the WRF simulations over these two selected periods provide useful information to guide the
142 selection of the free parameter α in MCSP for its GCM applications.

143 An algorithm of convective-stratiform separation in radar data analysis was adopted for
144 convective-stratiform heating partitioning. As detailed in Steiner et al. [1995] and Houze [2014], the
145 procedure is to first identify convective area, and then the remaining part of a studied area is treated as
146 stratiform region. The philosophy for determining convective region is based on the intensity and
147 peakness criteria in the reflectivity field. Specifically, any grid point either with at least 40dBZ or
148 exceeding the surrounding background reflectivity by a specified factor is considered a convective center.
149 Additionally, grid points surrounding a convective center, as described in Steiner et al. [1995], are
150 considered a convective area. A caveat of this approach is its inability to identify a shallow convective
151 area.

152 By using the aforementioned algorithm to analyze the WRF simulations conducted, the
153 convective-stratiform heating partitioning is obtained. As illustrated in Fig. 5, it is found that shallow
154 stratiform heating is approximately 0.3 to 0.5 that of the deep convective heating in both Indian Ocean
155 and the western Pacific. Therefore, α in Eq. 1 is assumed to be 0.3 and 0.5 in this study.

156 Since a favorable condition for the development of MCS includes substantial vertical wind shear,
157 we add a wind shear threshold in order to determine where MCSP is triggered. To examine the sensitivity
158 of the simulated climate on the wind shear threshold, we performed simulations with the zonal wind shear
159 between surface and 600 hPa set to exceed 0, 3, 5, and 7.5 m/s as the trigger. This condition ensures that
160 MCSP does not alter convective activities where the possibility of MCS formation is low. This is an
161 update to the formulation of MLB17.

162 4 Climate Model Simulations

163 a) Model Description

164 The climate model employed in this study is the Energy Exascale System Model, version 1
165 (E3SMv1) [Golaz et al., 2019], which originated from the Community Earth System Model version 1
166 (CESM1). There are significant developments in all individual components of the model compared to
167 CESM1 including: 1) new options for representing soil hydrology and biogeochemistry in the land model
168 (ELM) based on the Community Land Model version 4.5 (CLM4.5), 2) new ocean and sea-ice
169 components based on the Model for Prediction Across Scales (MPAS) framework, and 3) a new river
170 model (i.e., Model for Scale Adaptive River Transport (MOSART)) that has not been previously used in a
171 coupled Earth System Model.

172

173 Several updates to the atmospheric component of E3SMv1, EAMv1, are built upon the
174 Community Atmosphere Model version 5.3 (CAM5.3). EAMv1 employs a unified treatment of planetary
175 boundary layer turbulence, shallow convective, and cloud macrophysics with a third-order turbulence
176 closure parameterization (CLUBB; Cloud Layers Unified by Binormals) [Golaz et al., 2002; Larson and
177 Golaz, 2005; Larson, 2017] which eliminates unrealistic separation of these physical processes.
178 Turbulence, clouds, and convective processes are handled by the Zhang and McFarlane (ZM) deep
179 convection scheme [Zhang and McFarlane, 1995] paired with CLUBB and an updated cloud
180 microphysical scheme, version 2 of Morrison and Gettelman (MG2) [Morrison and Gettelman, 2008;
181 Gettleman and Morrison, 2015; Gettelman et al., 2015]. An update to the MG2 is a Classical Nucleation
182 Theory (CNT) based on ice nucleation (IN) parameterization for heterogeneous ice formation in mixed
183 phase clouds [Wang et al., 2014]. Rasch et al. [2019] provide an overview of EAMv1, while Xie et al.
184 [2018], Qian et al. [2018], and Zhang et al. [2019] show simulated cloud and convective characteristics
185 and the rationale for model tuning and Tang et al. [2019] documents its regionally refined capability for
186 developing high-resolution physics parameterizations.

187

188 The horizontal resolution of the simulations is ~100 km and there are 72 vertical levels with the
189 model top at 60 km. The configuration of the vertical grid is shown in Fig. 1 of Xie et al. [2018] with
190 vertical spacing in the upper troposphere and lower stratosphere ~600 m.

191 b) Simulations

192 We carried out six simulations with the stand alone atmospheric component of E3SM (EAMv1)
193 with prescribed observed sea-surface temperatures and sea-ice concentrations ('AMIP' simulations) and

194 four simulations with the fully coupled version of E3SMv1 ('Coupled' simulations). All simulations are
 195 30 years, beginning in November 1980 and ending in December 2009.

196

197 In these simulations we vary the parameter alpha (α) as well as the wind shear trigger (tunable
 198 parameters). The simulations are summarized in Table 1.

199

200 Table 1: Experimental set-up. All simulations are 30 years long from 1980 to 2009.

	Simulation Type	α	Wind shear trigger (m/s)
EAMv1	AMIP	0	0
EAMv1_a300	AMIP	0.3	0
EAMv1_a500	AMIP	0.5	0
EAMv1_a530	AMIP	0.5	3
EAMv1_a550	AMIP	0.5	5
EAMv1_a575	AMIP	0.5	7.5
E3SMv1	Coupled	0	0
E3SMv1_a300	Coupled	0.3	0
E3SMv1_a500	Coupled	0.5	0
E3SMv1_a530	Coupled	0.5	3

201

202 c) Results

203 We document the most significant impacts to EAMv1/E3SMv1 simulations due to MCSP as
 204 follows.

205

206 **(i) Deep Convection**

207 The heating rate of MCSP and its impact on the deep convection scheme are illustrated in Fig. 6.
 208 As shown in Fig. 2b, when deep convection occurs, the circulation of MCSs induces lower-tropospheric
 209 cooling and upper-tropospheric warming. The amplitude of MCSP heating alone is illustrated in Fig 6a
 210 for $\alpha=0.3$ and $\alpha=0.5$. With $\alpha=0.3$ ($\alpha = 0.5$) the lower tropospheric cooling peaks at 0.7 K/day (1.2
 211 K/day), where as the mid-tropospheric heating peaks at 0.25 K/day (0.5 K/day). MCSP produces
 212 temperature tendencies in the EAMv1 simulations that reflect the impact of MCSs. However, it is
 213 important to note that the heating tendencies illustrated in Fig. 6a are averaged per occurrence of deep

214 convection. Thus, the asymmetry in the magnitude of cooling and heating tendencies in the vertical
215 profile implies that there is more frequent occurrence of shallower convection which results in stronger
216 averaged cooling in the lower troposphere. Also notice that MCSP, by design, has a zero vertically
217 integrated temperature (dry static energy) tendency as a correction term is added to the column to ensure
218 the parameterization conserve total energy, and thus there is shallower but more intense cooling in the
219 lower troposphere and deeper and weaker warming in the upper troposphere.

220

221 The heating rate from the Zhang and McFarlane (ZM) [Zhang and McFarlane 1995] deep
222 convection scheme, with and without MCSP included, is shown in Fig. 6b. With the addition of MCSP,
223 the ZM heating rate is weaker in the lower troposphere because MCSP cools the lower troposphere.
224 However, the heating rate in the upper troposphere is also weaker than the control simulation where
225 MCSP adds heating (as will be explained below). Moreover, with a larger α the heating rate becomes
226 weaker in the upper troposphere which is somewhat surprising since MCSP provides a heating tendency.

227

228 The implication of the circulation associated with MCSs is to stabilize the troposphere since it has
229 a cooling effect in the lower troposphere and a heating effect aloft. Thus, when deep convection occurs,
230 MCSP reduces convective available potential energy (CAPE) by enhancing the tropospheric stability
231 making convection less persistent and less frequent. Hence, the additional MCSP heating has a
232 destabilizing effect leading to reduced deep convection, and reduced ZM heating. With a larger α , the
233 weakening of the heating rate by the deep convection scheme is more pronounced.

234

235 (ii) Tropical Variability

236

237 One well documented bias in E3SMv1 is the representation of tropical variability. In particular,
238 the Kelvin waves are much weaker than observations [Richter et al. 2019, Rasch et al. 2019]. As
239 described in Richter et. al [2014], Kelvin waves are an important driver of the quasi-biennial oscillation
240 (QBO). As illustrated in Fig 7b, the baseline model of EAMv1 indeed simulates much weaker Kelvin
241 waves than TRMM observations (Fig. 7a).

242

243 Importantly, MCSP enhances the Kelvin wave spectra in all simulations. The most pronounced
244 increase in Kelvin wave activity occurs when there is no wind shear trigger threshold in MCSP so it gets
245 activated whenever deep convection occurs. With a wind shear trigger, MCSP is activated less frequently
246 and therefore has a weaker impact on the simulation.

247

248 **(iii) MJO**

249 The MJO is a dominant mode of subseasonal variability in the tropics. The key signature of MJO
250 is eastward propagation of tropical convection originating from the Indian Ocean to the west Pacific
251 during the boreal winter [Madden and Julian 1971; Madden and Julian 1972]. The MJO is often not well
252 represented in climate models [Ahn et al. 2017; Ahn et al. 2020]. In observations, the cross-lag correlation
253 of precipitation shows pronounced eastward propagation from 60E to 160E and meridional propagation
254 from the equator to 20S and 20N (Fig. 8a).

255
256 The cross-lag correlation, of precipitation and zonal wind at 850 hP, indicates that the baseline
257 EAMv1 produces substantial westward precipitation (top panel of Fig. 8b) instead of eastward
258 propagation (top panel of Fig. 8a) in the Indian Ocean basin from the ERA-Interim reanalysis. This
259 indicates that there is substantial westward propagation component in the baseline model. The observation
260 indicates that there is nearly symmetrical meridional propagation, extending to 20 S/N from the equator in
261 precipitation (bottom panel of Fig. 8a). However, EAMv1 simulates much less meridional propagation in
262 the Indian Ocean basin (bottom panel of Fig. 8b).

263
264 With MCSP, EAMv1 simulates less westward propagation and more meridional propagation (Fig
265 8b c-g). The setup with $\alpha = 0.5$ and wind shear threshold = 3 m/s (Fig. 8e) shows significant
266 improvement over the baseline model since the simulation shows the clearest eastward propagation in
267 precipitation.

268
269 When run in the fully coupled configuration (E3SMv1), the model shows significant
270 improvement over EAMv1 in simulating the MJO. The fully coupled model produces clear eastward
271 propagation of precipitation in the Indian Ocean basin (Fig. 9a) and removes most of the westward
272 propagation occurring in EAMv1 (Fig. 8b). However, meridional precipitation propagation in E3SMv1 is
273 still weak compared to observation. With inclusion of MCSP, the eastward precipitation propagation is
274 faster than the baseline E3SMv1 (Fig. 9b) when $\alpha = 0.5$ (Fig. 9c,d). MCSP also extends meridional
275 propagation farther from the equator.

276
277 The spectral characteristics of the MJO are considered in Figures 10 and 11. Observations (Fig.
278 10a) show eastward propagation in outgoing longwave radiation (OLR) in the Indian Ocean with a period
279 between 30 and 90 days and wave numbers between 1 and 3 during the boreal winter. The baseline
280 EAMv1 has little power between 30 and 90 days in eastward propagation (Fig. 10b) despite substantial
281 eastward propagation for periods greater than 90 days. In addition, there is slow (>90 days) westward

282 propagation in the baseline model.

283

284 When MCSP is included in EAMv1, slow (>90 days) eastward propagation of OLR is further
285 enhanced (Fig. 10 c-g). However, more power within the window of 30-90 days in eastward propagation
286 is evident in Fig. 10 c-e, implying that the simulated MJO is improved. It is worth noting that Fig. 10e
287 shows much stronger westward propagation which indicates degradation from the baseline model
288 simulation.

289

290 E3SMv1 indicates an improved MJO compared to EAMv1 in terms of increased power within
291 the window of 30-90 days in eastward propagation as shown in Fig. 11a, although the eastward
292 propagation is still too slow compared to observation (Fig. 10a). With MCSP, the fully coupled model
293 simulations (Fig. 11b-d) show further improvements, i.e., increased power in the 30-90 day window in
294 eastward propagation whilst not enhancing westward propagation. The MJO spectra is too strong for $\square =$
295 0.5 without a wind shear threshold (Fig.11c), but is reduced by a wind shear trigger threshold of 3 m/s
296 (Fig. 11d).

297

298 Figure 12 illustrates the life-cycle composite of MJO revealing that EAMv1 simulates much
299 weaker OLR (Fig. 12 b). With MCSP, the intensity of OLR is enhanced slightly but still much weaker
300 than observation. Additionally, EAMv1, without or with MCSP, also lacks organized convection within
301 the Indian Ocean basin during phases 2 and 3, compared to observation (Fig. 12a).

302 Figure 13a shows E3SMv1 simulates stronger OLR, but the lack of organized convection in the
303 Indian Ocean basin during phases 2 and 3 still persists. With MCSP (Fig. 13b,c,d), the intensity of OLR
304 is stronger, mainly in the later phases (5-8) but the model also fails to produce strong organized
305 convection in the Indian Ocean basin during phases 2 and 3.

306

307 **(iv) Precipitation Biases**

308 Since MCSP is implemented within the deep convection scheme, it is anticipated to alter
309 convective precipitation especially in the lower latitudes where active deep convection is extensive.
310 Indeed, MCSP mainly modifies precipitation near the tropics and subtropics in both EAMv1 (Fig. 14) and
311 E3SMv1 (Fig.15). In both model configurations, MCSP robustly reduces precipitation around the
312 tropical east Pacific, Colombia, and Ecuador (see Fig. 14, 15). The reduction of precipitation in these
313 regions is more pronounced when the wind shear threshold is set smaller, meaning that MCSP is triggered
314 more frequently. Also, these regions are where the baseline EAMv1/E3SMv1 produces positive biases in
315 precipitation so MCSP provides an improvement. Nevertheless, the reduction is weaker during

316 December-January-February (DJF), a feature also evident in CAM5.5 simulations, i.e. Fig. 14b of
317 MLB17.

318
319 The annual average of the EAMv1 simulations with MCSP shares several other features found in
320 CAM5.5 (e.g., Fig. 14b in MLB17), such as enhancement in precipitation in the tropical west Pacific,
321 south China sea, and Indian Ocean basin, and reduction in tropical Africa (see Fig. 14d). Such features are
322 suppressed with a higher wind shear trigger (Fig. 14 b,c). It is also worth noting that the enhancement in
323 precipitation in south China sea and the Indian Ocean is mainly attributed to DJF (Figs. 14 g,h) since in
324 June-July-August (JJA, see Figs. 14 k,l), the change in precipitation in these regions due to MCSP is
325 negative. However, these features represent a degradation to EAMv1 because the baseline model already
326 simulates positive biases in precipitation in these regions (Fig. 14a).

327
328 Another region seen significant change in precipitation due to MCSP is in south and southeast
329 Asia, and over India and Indian Ocean basin. In DJF, a reduction in precipitation due to MCSP is found
330 (Fig. 14j,k,l and Fig. 15j,k,l). EAMv1 and E3SMv1 in the baseline model configuration both produce
331 positive biases in these regions and thus such changes in DJF make the simulated climate closer to
332 observation.

333
334 When MCSP is incorporated in the fully coupled model, E3SMv1, the change in
335 precipitation in the tropical west Pacific differs from those in EAMv1. For the annual average, a reduction
336 in precipitation occurs (Figs. 15 b,c,d), which improves the model biases. However, E3SMv1 with MCSP
337 simulates more precipitation in these regions in DJF (Figs. 15 f,g,h) and thus degrades the model. The
338 reduction in annual precipitation is thus attributed to more pronounced lower precipitation simulated in
339 JJA (Figs. 15 j,k,l).

340
341 In terms of annual precipitation, MCSP does not induce a coherent feature in the tropical west
342 Pacific between EAMv1 and E3SMv1. However, the parameterization induces the same features in
343 seasonal averages: MCSP enhances precipitation in DJF but reduces precipitation in JJA in these regions.

344

345 **5 Summary and Conclusions**

346 We implemented MCSP in E3SMv1 with modifications from its original form and investigated
347 its impact on the simulated climate in AMIP and coupled simulations. MCSP represents the important
348 organized physical and dynamical processes induced by the MCS circulation in the form of lower-
349 tropospheric cooling and upper-troposphere heating. The intensity of the cooling and heating is

350 proportional to the column integral of heating by deep convection revealed by convection resolving WRF
351 simulations. Specifically, when deep convection occurs, MCSP decreases the convective available
352 potential energy by enhancing the tropospheric static stability, acting to suppress subsequent convection .
353

354 Modeling efforts have attempted to improve the simulated MJO in climate models in recent years.
355 Implementation of MCSP in E3SMv1 provides significant improvement in MJO simulation in terms of
356 stronger eastward propagation of precipitation and OLR in the Indian Ocean basin and increased power in
357 the eastward spectra for periods between 30 and 90 days. This suggests that convection over this region,
358 as simulated by the baseline model, is over-persistent and hinders propagation. Since MCSP stabilizes the
359 troposphere when deep convection occurs, it shortens the duration of convection within a grid-cell and
360 helps the persistent propagation of coherent convective systems.
361

362 In the simulated climate, MCSP reduces precipitation over the tropical western Pacific,
363 Colombia, and Ecuador, where the baseline model simulates too much precipitation. This feature is
364 independent of the model configurations and implies that the baseline model may have too-persistent deep
365 convection in these regions. With MCSP removing some CAPE, it may serve to improve precipitation
366 biases where deep convection is overly active in the baseline model.
367

368 Under the two model configurations examined in this study, different model behavior was found
369 in the annual precipitation around tropical west Pacific induced by MCSP: EAMv1 simulated higher
370 precipitation but E3SMv1 simulated lower precipitation. In further analysis, we found that MCSP
371 enhanced precipitation in these regions in DJF and reduced precipitation in JJA. This signature was not
372 dependent on the model configuration. Thus, it is evidently crucial to analyze the seasonal impact of
373 MCSP instead of focusing on only the annual average since its impact can reverse sign depending on the
374 season.
375

376 Herein we limited the scope of our investigation to the effects of mesoscale convective heating as
377 represented by MCSP on the simulated global climate. However, momentum transport is another
378 important feature of organized moist convection that requires investigation. Note that, in an atmosphere-
379 only model context, MLB17 compared the effects of MCSP convective heating and convective
380 momentum transport and discovered interesting differences in a global context. In our future MCSP work,
381 we will explore and compare the effects of convective momentum transport and convective heating in the
382 atmosphere-only and coupled versions of E3SM.
383

384 **Acknowledgements:**

385 This research was supported by DOE's Office of Biological and Environmental Research (BER),
386 Earth and Environmental System Modeling program and the Energy Exascale Earth System Model
387 (E3SM) project for its next generation of development (NGD) of atmospheric physics, funded by the
388 DOE, Office of Science, BER. This research used resources of the National Energy Research Scientific
389 Computing Center, a DOE Office of Science User Facility supported by the Office of Science of the U.S.
390 DOE under Contract No. DE-AC02-05CH11231. This material is based upon work supported by the
391 National Center for Atmospheric Research, which is a major facility sponsored by the National Science
392 Foundation under Cooperative Agreement No. 1852977. Work at LLNL was performed under the
393 auspices of the U.S. DOE by Lawrence Livermore National Laboratory under contract DE-AC52-
394 07NA27344. The Pacific Northwest National Laboratory is operated for the U.S. DOE by Battelle
395 Memorial Institute under contract DE-AC05-76RL01830. Output from the default E3SMv1 simulations
396 can be downloaded via the following link: https://portal.nersc.gov/project/e3sm/cchen24/MCSP_JAMES/
397

398 **References**

- 399 Ahn, M.-S., Kim, D., Sperber, K.R., Kang, I.-S., Maloney, E., Waliser, D., and Hendon, H., 2017: MJO
400 simulation in CMIP5 climate models: MJO skill metrics and process-oriented diagnosis. *Clim Dyn*
401 49, 4023–4045, <https://doi.org/10.1007/s00382-017-3558-4>
- 402 Ahn, M.-S., Kim, D., Kang, D., Lee, J., Sperber, K. R., Gleckler, P. J., Jiang, X., Ham, Y.-G., and Kim,
403 H., 2020: MJO propagation across the Maritime Continent: Are CMIP6 models better than CMIP5
404 models? *Geophys. Res. Lett.*, 47, e2020GL087250. <https://doi.org/10.1029/2020GL087250>
- 405 Chen, B., and B. E. Mapes, 2018: Effects of a simple convective organization scheme in a two-plume
406 gcm. *J. Adv. Model Earth Syst.*, 10(3):867–80.
- 407 D'Andrea, F., P. Gentile, A. K. Betts, B. R. Lintner, 2014: Triggering deep convection with a
408 probabilistic plume model. *J. Atmos. Sci.*, 71:3881–901. <https://doi.org/10.1175/JAS-D-13-0340.1>.
- 409 Golaz, J.-C., P. M. Caldwell, L. P. Van Roekel, M. R. Petersen, Q. Tang, J. D. Wolfe, et al., 2019: The
410 DOE E3SM coupled model version 1: Overview and evaluation at standard resolution. *Journal of*
411 *Advances in Modeling Earth Systems*, 11, 2089–2129. <https://doi.org/10.1029/2018MS001603>.
- 412 Golaz, J.-C., V. E. Larson, and W. R. Cotton, 2002: On a PDF-based model for boundary layer clouds.
413 Part I: Method and model description. *J. Atmos. Sci.*, 59(24), 3540–3551.
- 414 Hong, S. and Lim, J., 2006: The WRF single-moment 6-class microphysics scheme (WSM6). *Journal of*
415 *the Korean Meteorological Society*, 42, 129-151.
- 416 Hong, S.-Y., Y. Noh, and J. Dudhia, 2006: A new vertical diffusion package with an explicit treatment of
417 entrainment processes. *Mon. Wea. Rev.*, 134, 2318–2341, doi:10.1175/MWR3199.1.

418 Houze, R. A., Jr., 2004: Mesoscale convective systems. *Rev. Geophys.*, **42**, RG4003,
419 doi:10.1029/2004RG000150.

420 Houze, R. A., Jr., 2014: Cloud Dynamics. 2nd ed. *International Geophysics Series*, Vol. 14, Academic
421 Press, 432 pp.

422 Gettelman, A., and H. Morrison, 2015: Advanced two-moment bulk microphysics for global models. Part
423 I: Off-line tests and comparison with other schemes. *J. Climate*, **28**(3), 1268–1287.
424 <https://doi.org/10.1175/JCLI-D-14-00102.1>.

425 Gettelman, A., H. Morrison, S. Santos, P. Bogenschutz, and P. M. Caldwell, 2015: Advanced two-
426 moment bulk microphysics for global models. Part II: Global model solutions and aerosol-cloud
427 interactions. *J. Climate*, **28**(3), 1288–1307. <https://doi.org/10.1175/JCLI-D-14-00103.1>

428 Iacono, M. J., J. S. Delamere, E. J. Mlawer, M. W. Shephard, S. A. Clough, and W. D. Collins, 2008:
429 Radiative forcing by longlived greenhouse gases: Calculations with the AER radiative
430 transfer models. *J. Geophys. Res.*, **113**, D13103, doi:10.1029/2008JD009944.

431 Larson, V. E., 2017: CLUBB-SILHS: A parameterization of subgrid variability in the atmosphere.
432 ArXiv:1711.03675 [Physics].

433 Larson, V. E., and J. C. Golaz, 2005: Using probability density functions to derive
434 consistent closure relationships among higher-order moments. *Mon. Wea. Rev.*, **133**(4), 1023–1042.
435 <https://doi.org/10.1175/MWR2902.1>.

436 Madden, R. A., and Julian, P. R., 1971: Detection of a 40–50 day oscillation in the zonal wind in the
437 tropical Pacific. *Journal of the Atmospheric Sciences*, **28**(5), 702–708. <https://doi.org/10.1175>

438 Madden, R. A., and Julian, P. R., 1972: Description of global-scale circulation cells in the tropics with a
439 40–50 day period. *Journal of the Atmospheric Sciences*, **29**(6), 1109–1123. <https://doi.org/10.1175>

440 Moncrieff, M.W., 1992: Organized convective systems: Archetypal models, mass and momentum flux
441 theory, and parameterization. *Quart. J. Roy. Meteorol. Soc.*, **118**, 819–850.

442 Moncrieff, M. W., 1995: Mesoscale convection from a large-scale perspective. *Atmos. Res.*, **35**, 87–112.
443 [https://doi.org/10.1016/0169-8095\(94\)00012-3](https://doi.org/10.1016/0169-8095(94)00012-3)

444 Moncrieff, M. W., and C. Liu, 2006: Representing convective organization in prediction models by a
445 hybrid strategy. *J. Atmos. Sci.*, **63**, 3404–3420, doi:10.1175/JAS3812.1.

446 Moncrieff, M. W., C. Liu, and P. Bogenschutz, 2017: Simulation, modeling, and dynamically based
447 parameterization of organized tropical convection for global climate models. *J. Atmos. Sci.*, **74**, 1363-
448 1380, doi:10.1175/JAS-D-16-0166.1.

449 Morrison, H., and A. Gettelman, 2008: A new two-moment bulk stratiform cloud microphysics scheme in
450 the Community Atmosphere Model, version 3 (CAM3). Part I: Description and numerical tests. *J.*
451 *Climate*, **21**(15), 3642–3659.

452 Nesbitt, S. W., R. Cifelli, and S. A. Rutledge, 2006: Storm morphology and rainfall characteristics of
453 TRMM precipitation features, *Mon. Wea. Rev.*, **134**, 2702-2721, doi:10.1175/MWR3200.1.

454 Niu, G.-Y., Z.-L. Yang, K. E. Mitchell, F. Chen, M. B. Ek, M. Barlage, A. Kumar, K. Manning, D.
455 Niyogi, E. Rosero, M. Tewari, and Y. Xia, 2011: The community Noah land surface model with
456 multiparameterization options (Noah-MP): 1. Model description and evaluation with local-scale
457 measurements. *J. Geophys. Res.*, **116**, D12109, doi: 10.1029/2010JD015139.

458 Qian, Y., H. Wan, B. Yang, J.-C. Golaz, B. Harrop, Z. Hou, et al., 2018: Parametric sensitivity and
459 uncertainty quantification in the version 1 of E3SM atmosphere model based on short perturbed
460 parameter ensemble simulations. *J. Geophys. Res.*, **123**, 13,046–13,073.
461 <https://doi.org/10.1029/2018JD028927>

462 Rasch, P. J., S. Xie, P.-L. Ma, W. Lin, H. Wang, Q. Tang, et al. (2019). An overview of the atmospheric
463 component of the Energy Exascale Earth System Model. *Journal of Advances in Modeling Earth*
464 *Systems*, **11**, 2377–2411. <https://doi.org/10.1029/2019MS001629>.

465 Richter, J. H., J. T. Bacmeister, and A. Solomon, 2014: On the simulation of the quasi-biennial oscillation
466 in the Community Atmosphere Model, version 5. *J. Geophys. Res.*, **119**, 3045–3062.
467 <https://doi.org/10.1002/2013JD021122>. Richter, J. H., C.-C. Chen, Q. Tang, S. Xie, and P. J. Rasch,
468 2019: Improved simulation of the QBO in E3SMv1. *Journal of Advances in Modeling Earth Systems*,
469 **11**, 3403–3418. <https://doi.org/10.1029/2019MS001763>.

470 Richter, J. H., and P. J. Rasch, 2008: Effects of convective momentum transport on the Atmospheric
471 Circulation Model, version 3. *J. Climate*, **21**, 1487-1499. Doi: 10.1175/2007JCLI1789.1

472 Skamarock, W. C., Klemp, J. B., Dudhia, J., Gill, D. O., Barker, D., Duda, M. G., and Powers, J. G.,
473 2008: A description of the advanced research WRF Version 3, No. NCAR/TN-475+STR, University
474 Corporation for Atmospheric Research, doi:10.5065/D68S4MVH.

475 Steiner, M., R. A. Houze Jr., and S. E. Yuter, 1995: Climatological characterization of three-dimensional
476 storm structure from operational radar and rain gauge data. *J. Appl. Meteor.*, **34**, 1978–2007.

477 Tang, Q., Klein, S. A., Xie, S., Lin, W., Golaz, J.-C., Roesler, E. L., Taylor, M. A., Rasch, P. J., Bader, D.
478 C., Berg, L. K., Caldwell, P., Giangrande, S. E., Neale, R. B.,

479 Qian, Y., Riihimaki, L. D., Zender, C. S., Zhang, Y., and Zheng, X.: Regionally refined test bed in E3SM
480 atmosphere model version 1 (EAMv1) and applications for high-resolution modeling, *Geosci. Model*
481 *Dev.*, **12**, 2679–2706, <https://doi.org/10.5194/gmd-12-2679-2019>, 2019.

482 Tao, W.-K., and M. W. Moncrieff, 2009: Multiscale cloud system modeling. *Rev. Geophys.*, **47**, RG4002,
483 doi:10.1029/2008RG000276.

484 Wheeler, M. and G. Kiladis, 1999: Convectively coupled equatorial waves: analysis of clouds and
485 temperature in the wavenumber-frequency domain. *J. Atmos. Sci.*, **56**(3): 374-300.
486 [https://doi.org/10.1175/1520-0469\(1999\)056<0374:CCEWAO>2.0.CO;2](https://doi.org/10.1175/1520-0469(1999)056<0374:CCEWAO>2.0.CO;2).

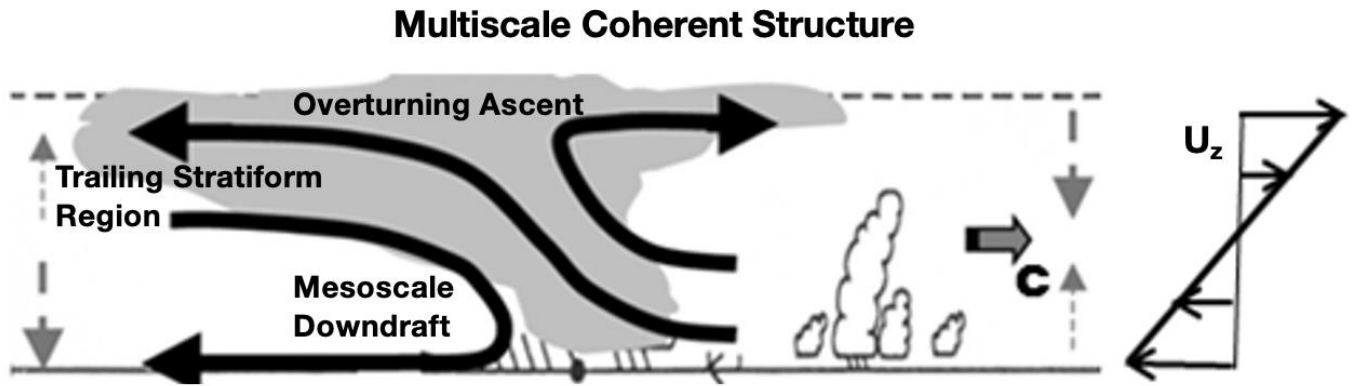
487 Xie, S., W. Lin, P. J. Rasch, P.-L. Ma, R. Neale, V. E. Larson, et al., 2018: Understanding cloud and
488 convective characteristics in version 1 of the E3SM atmosphere model. *Journal of Advances in*
489 *Modeling Earth Systems*, **10**, 2618–2644. <https://doi.org/10.1029/2018MS001350>.

490 Zhang, G. J., and N. A. McFarlane, 1995: Sensitivity of climate simulations to the parameterization of
491 cumulus convection in the Canadian Climate Centre General Circulation Model. *Atmosphere-Ocean*,
492 **3**, 407–446.

493 Zhang, Y., S. Xie, W. Lin, S. A. Klein, M. Zelinka, P.-L. Ma, et al., 2019: Evaluation of clouds in version
494 1 of the E3SM atmosphere model with satellite simulators. *Journal of Advances in Modeling Earth*
495 *Systems*, **11**, 1253–1268. <https://doi.org/10.1029/2018MS001562>.

496
497
498
499
500
501
502
503
504
505
506
507
508
509
510
511
512
513
514
515
516
517

518
519
520
521
522
523



524

525 **Figure 1:** Diagram of multiscale coherent structure with a slantwise overturning layer including a trailing
526 stratiform region, an overturning ascent, and a mesoscale downdraft.(adapted from MLB17) The structure
527 is propagating from left to right at speed 'C' in a sheared wind environment depicted by ' U_z '.

528

529

530

531

532

533

534

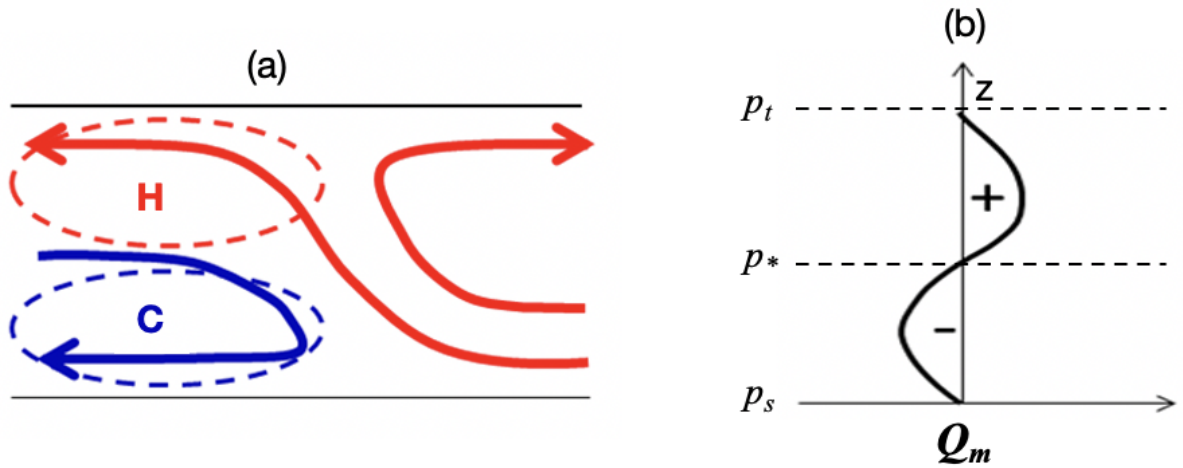
535

536

537

538

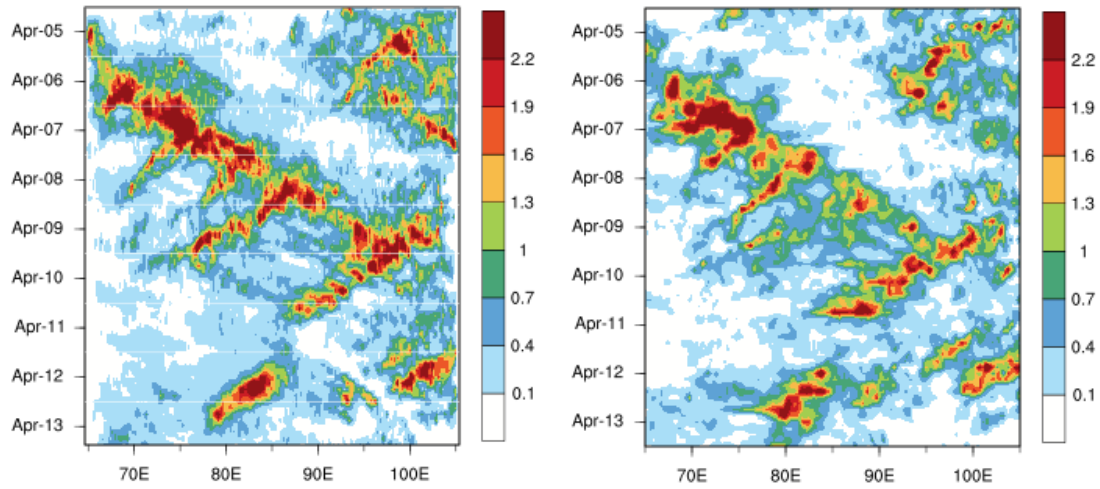
539
540
541
542



543
544
545
546
547
548
549
550
551
552
553
554
555
556
557
558
559
560
561
562
563

Figure 2: (a) Idealization of mesoscale heating (H) and cooling (C) regions of the prototype MSCP adopted for the prototype MCSP of Moncrieff et al. (2017). The heating/cooling dipole in (b) is consistent with the mesoscale ascent (thick red lines) and cool mesoscale descent (thick blue line) in (a). (adapted from Fig. 12 of MLB17)

564
565
566
567
568



569

570 **Figure 3:** Observed (left) and modeled (right) time-longitude distributions of 6.5°S-6.5°N averaged
571 hourly precipitation rate (mm h^{-1}) for 5-13 April 2009.

572

573

574

575

576

577

578

579

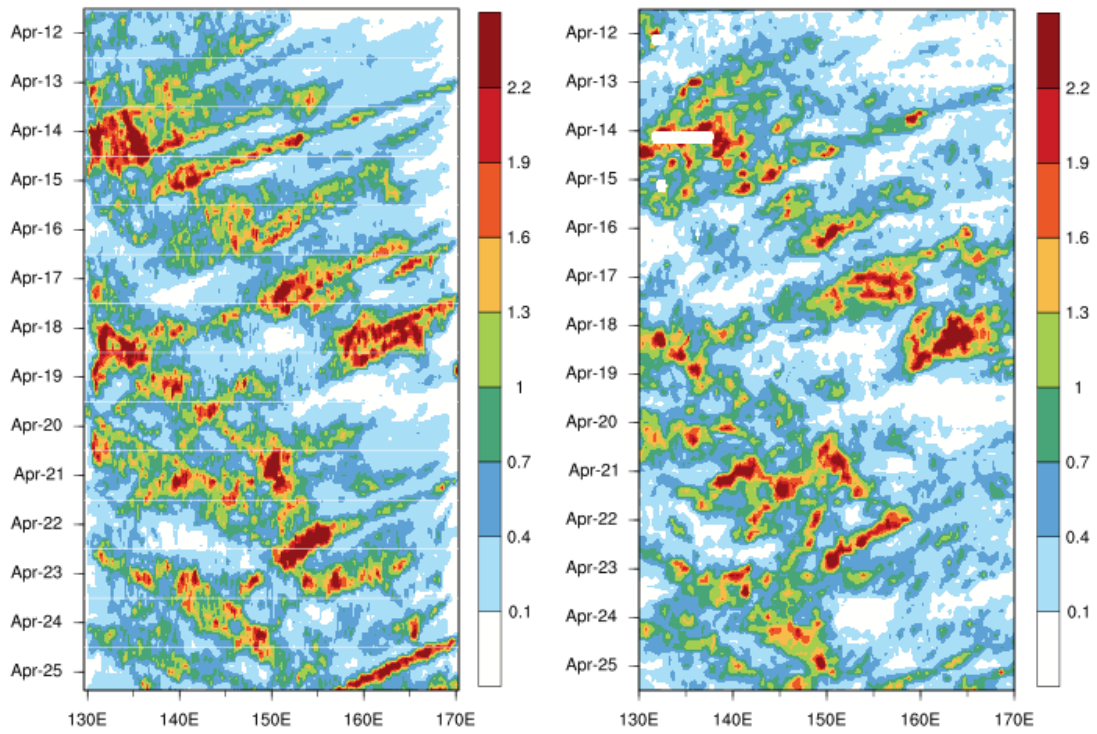
580

581

582

583

584



585

586 **Figure 4:** Observed (left) and modeled (right) time-longitude distributions of 5.5°S-7.5°N averaged
587 hourly precipitation rate (mm h^{-1}) for 12-25 April 2009.

588

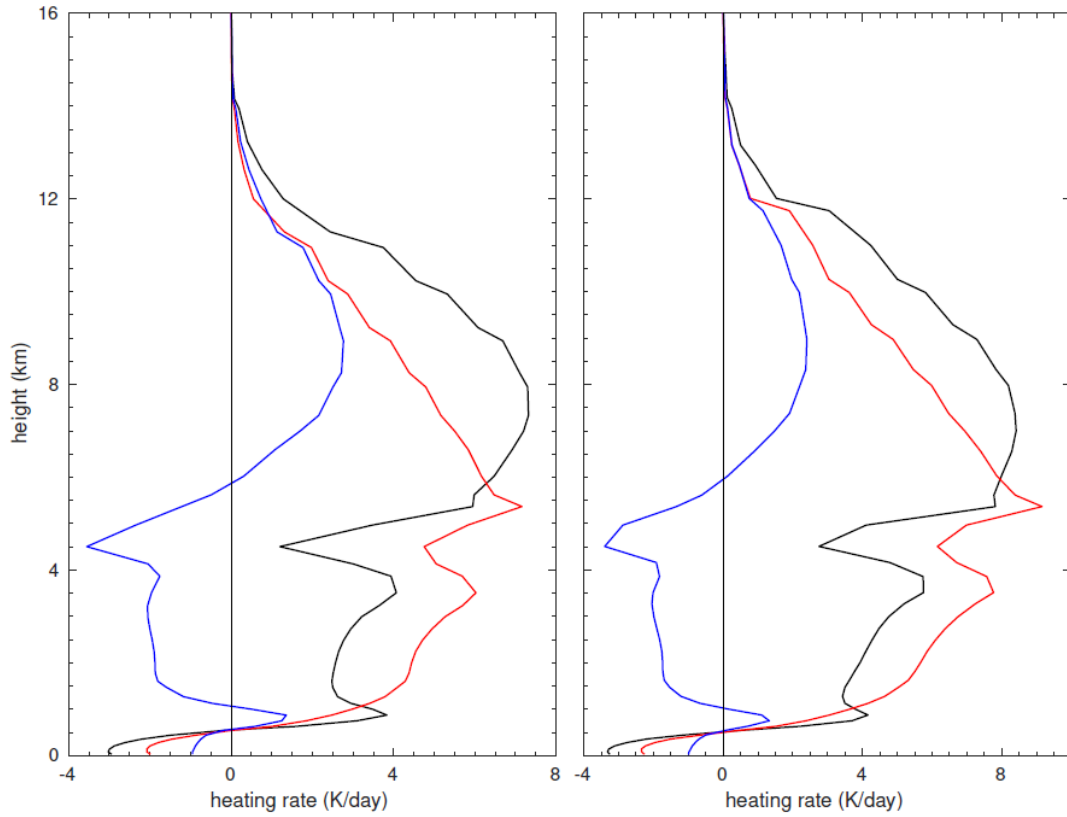
589

590

591

592

593



594

595 **Figure 5:** Heating profiles for deep convection (red), stratiform and shallow convection (blue), and their
 596 sum (black). The left and right panels are corresponding to the convective episode (5-13 April 2009) in
 597 the Indian Ocean and the convective episode (12-25 April 2009) in the western Pacific, respectively.

598

599

600

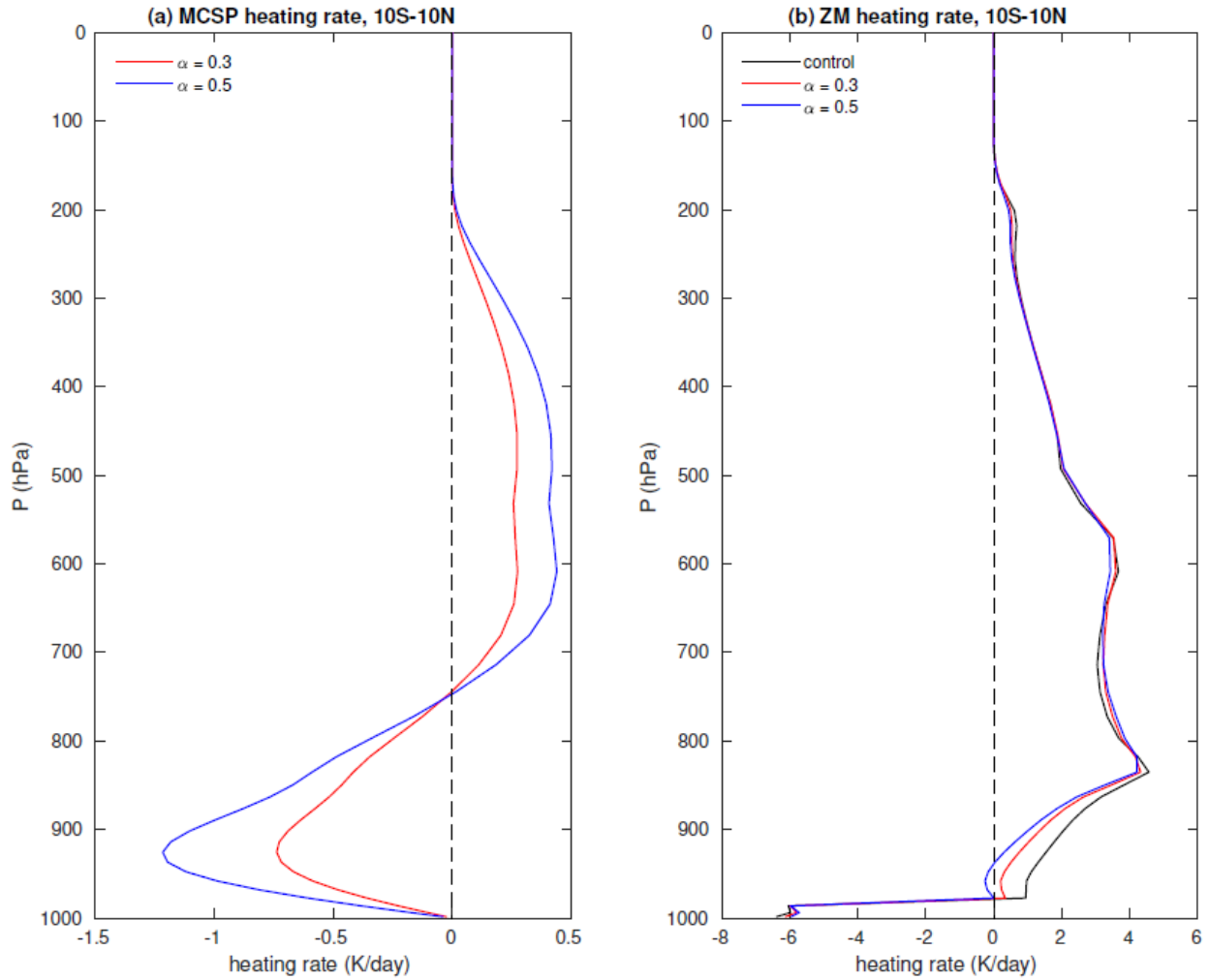
601

602

603

604

605



606

607 **Figure 6:** One-month (1980/11) averaged heating rate profile due to a) deep convection scheme with
 608 MCSP parameterization, and b) MCSP parameterization by EAMv1 simulations.

609

610

611

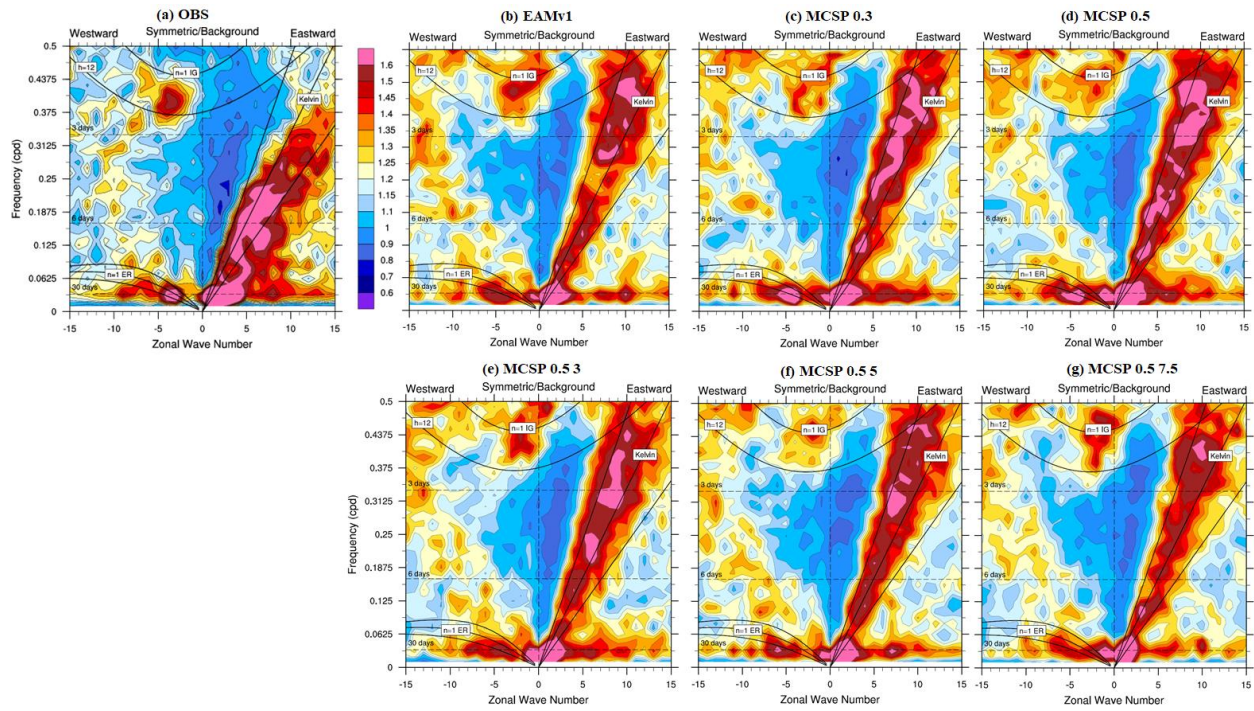
612

613

614

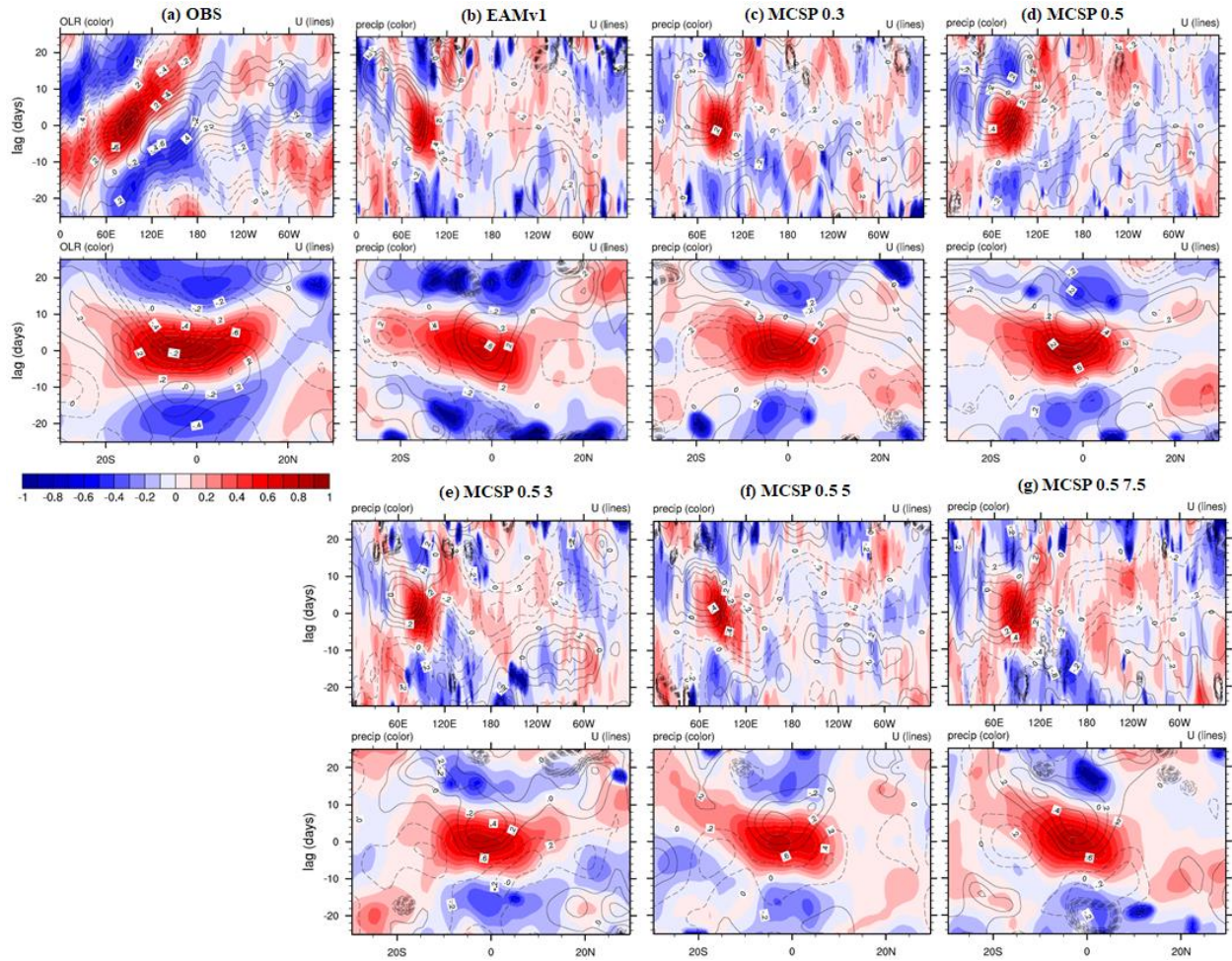
615

616



617
 618 **Figure 7:** Symmetric component of frequency-wavenumber power spectra of precipitation based on
 619 methodology of Wheeler and Kiladis (1999) for: a) TRMM, b) baseline EAMv1 simulation, c) EAMv1
 620 with MCSP and $\square = 0.3$, d) EAMv1 with MCSP and $\square = 0.5$, e) EAMv1 with MCSP and $\square = 0.5$, wind
 621 shear trigger = 3 m/s, f) EAMv1 with MCSP and $\square = 0.5$, wind shear trigger = 5 m/s, and g) EAMv1 with
 622 MCSP and $\square = 0.5$, wind shear trigger = 7.5 m/s.

623
 624
 625
 626
 627
 628
 629
 630
 631
 632
 633



634

635

636 **Figure 8:** Cross-lag correlation of precipitation and zonal wind at 850 hPa during the boreal winter by a)
 637 ERA-Interim, and simulations by EAMv1: b) baseline model, c) MCSP with $\square = 0.3$, d) MCSP with \square
 638 $= 0.5$, e) MCSP $\square = 0.5$ and a wind shear threshold of 3 m/s, f) MCSP $\square = 0.5$ and a wind shear
 639 threshold of 5 m/s, g) MCSP $\square = 0.5$ and a wind shear threshold of 7.5 m/s.

640

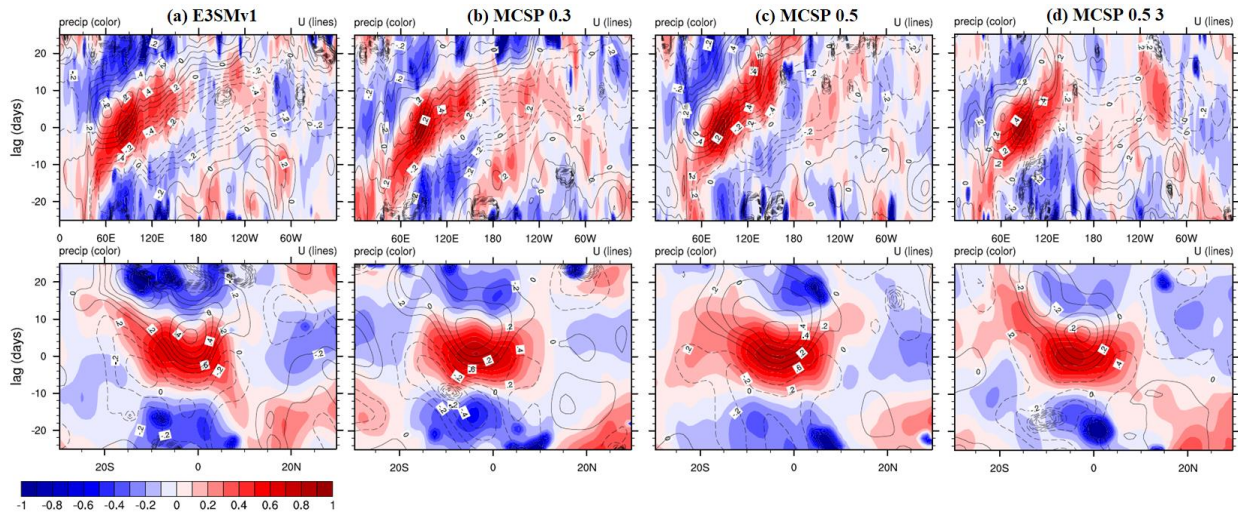
641

642

643

644

645



646

647 **Figure 9:** Cross-lag correlation during winter months in the northern hemisphere based on simulations of
 648 E3SMv1: a) baseline model, b) MCSP $\sigma = 0.3$, c) MCSP $\sigma = 0.5$, d) MCSP $\sigma = 0.5$ and a wind shear
 649 threshold of 3 m/s.

650

651

652

653

654

655

656

657

658

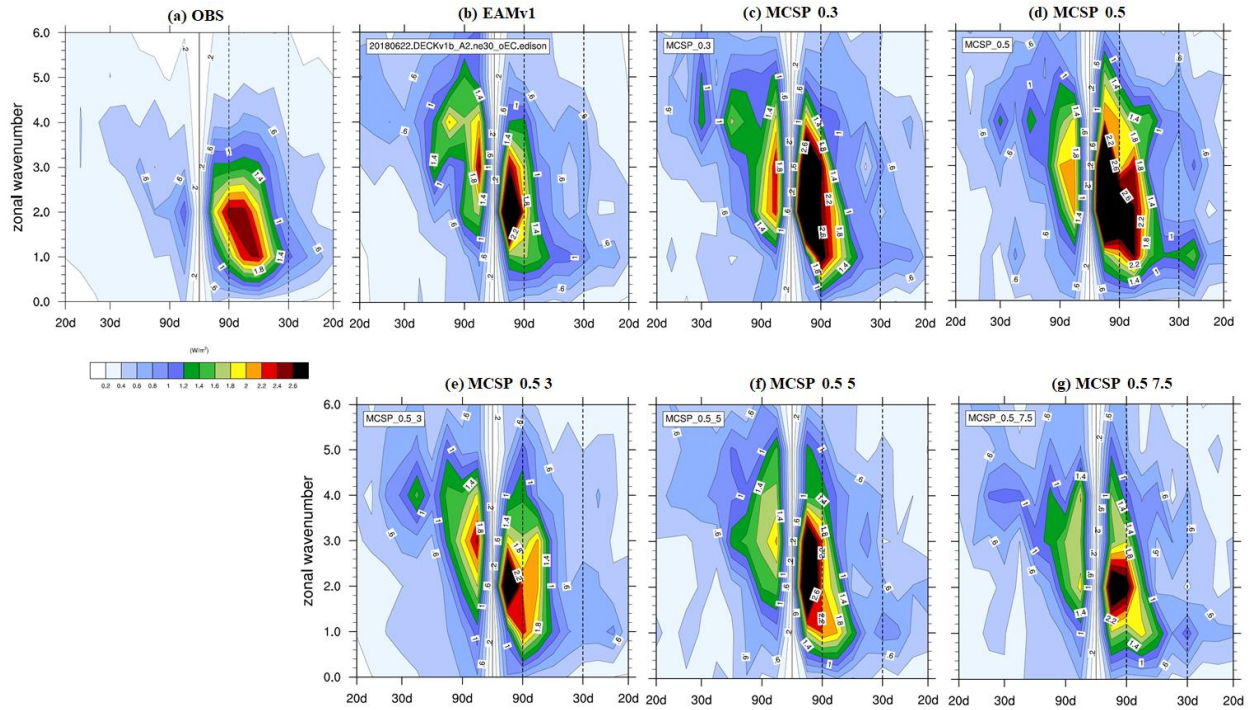
659

660

661

662

663



664

665 **Figure 10:** Same as Fig. 8, except for outgoing longwave radiation (OLR).

666

667

668

669

670

671

672

673

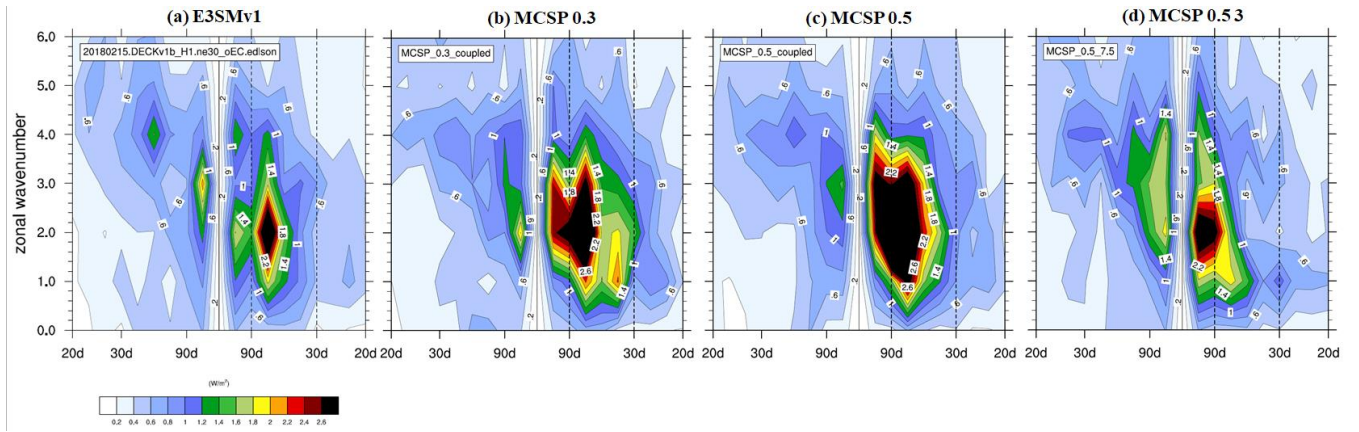
674

675

676

677

678



679

680 **Figure 11:** Same as Fig. 9, except for the spectra of OLR.

681

682

683

684

685

686

687

688

689

690

691

692

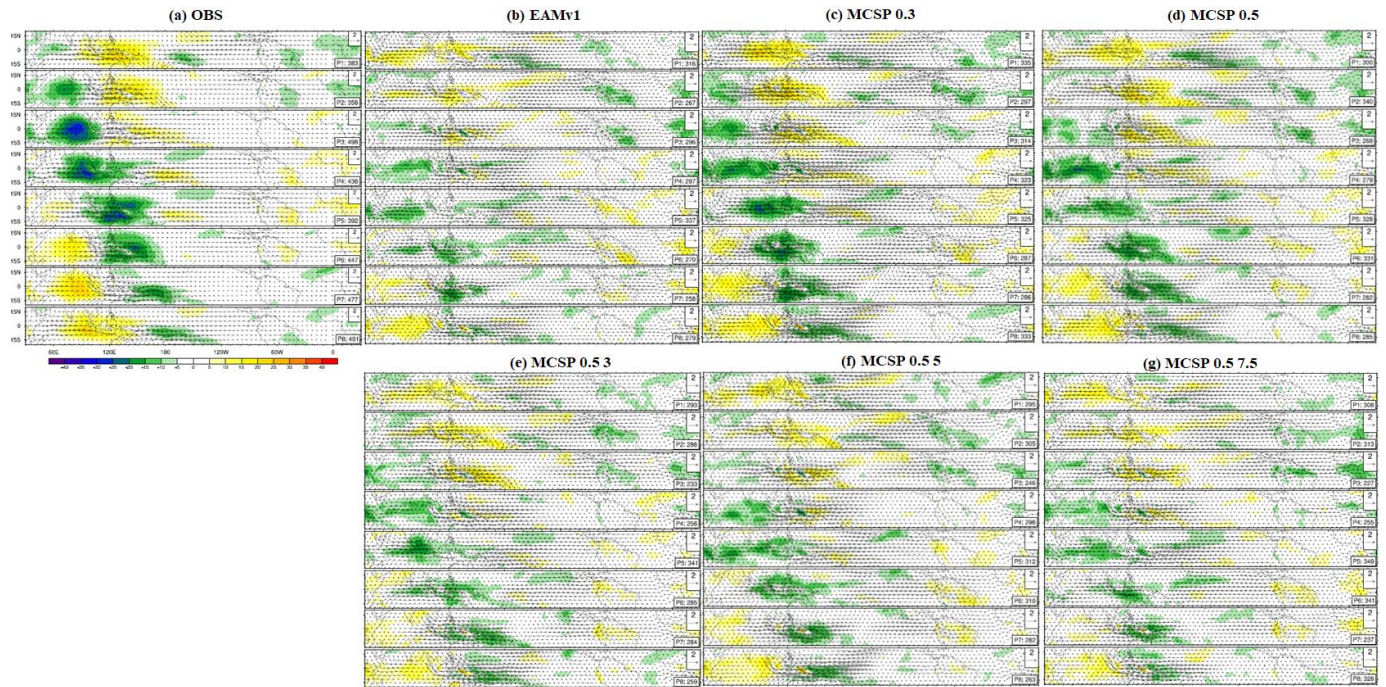
693

694

695

696

697



698

699 **Figure 12:** Life-cycle composite of MJO for the same simulations as those shown in Fig. 8.

700

701

702

703

704

705

706

707

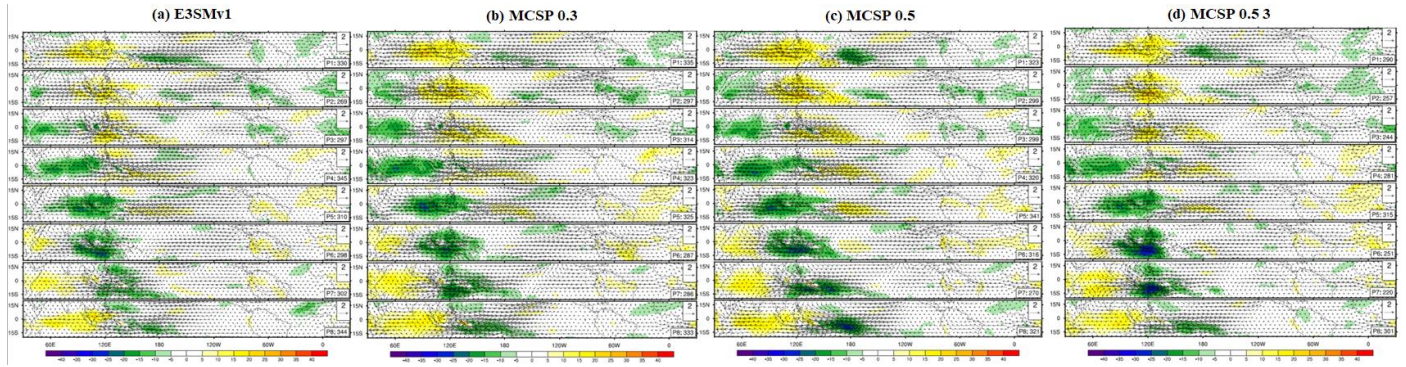
708

709

710

711

712



713

714 **Figure 13:** Life-cycle composite of MJO for the same simulations as those shown in Fig. 9.

715

716

717

718

719

720

721

722

723

724

725

726

727

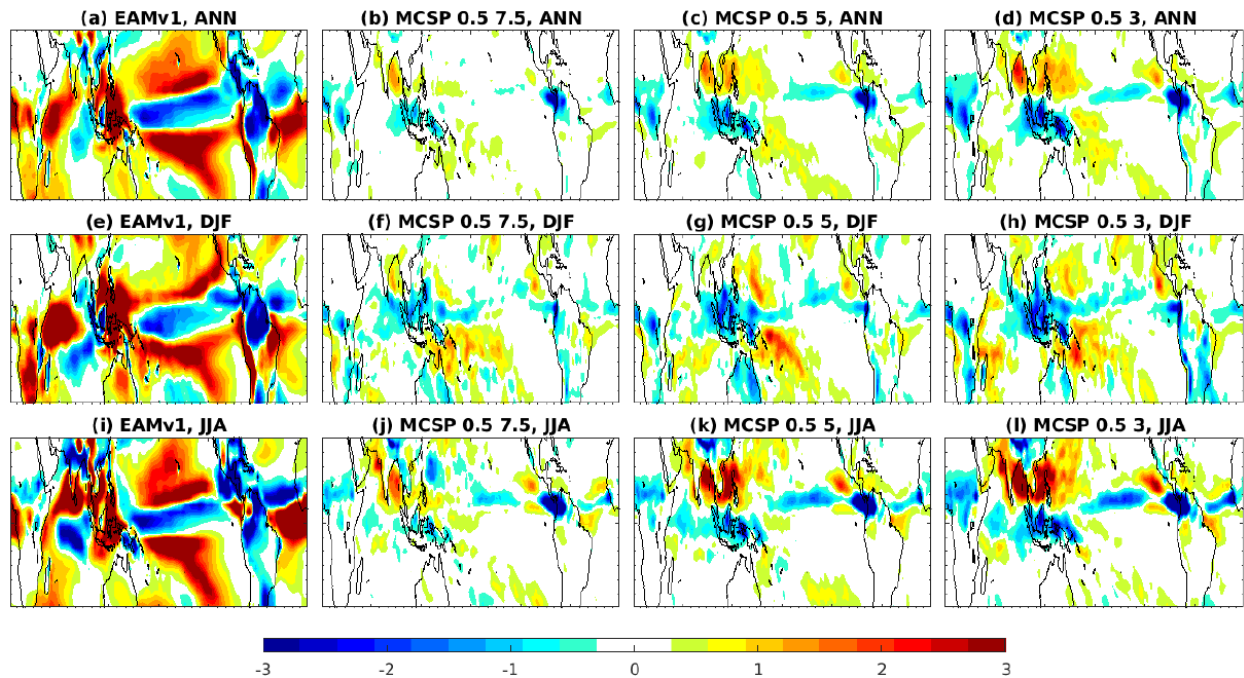
728

729

730

731

732



733

734 **Figure 14:** Precipitation biases (mm/day) simulated by EAMv1: 1) top panels as annual averages, 2)
 735 middle panel for DJF, and 3) bottom panels for JJA. The first column is for the baseline model against
 736 GPCP and the rest columns are for MCSP with various configurations against the baseline model. The
 737 second column is for MCSP with $\alpha = 0.5$ and a wind shear threshold 7.5 m/s, the third column is for
 738 MCSP with $\alpha = 0.5$ and a wind shear threshold 5 m/s, and the last column is for MCSP with $\alpha = 0.5$
 739 and a wind shear threshold 3 m/s.

740

741

742

743

744

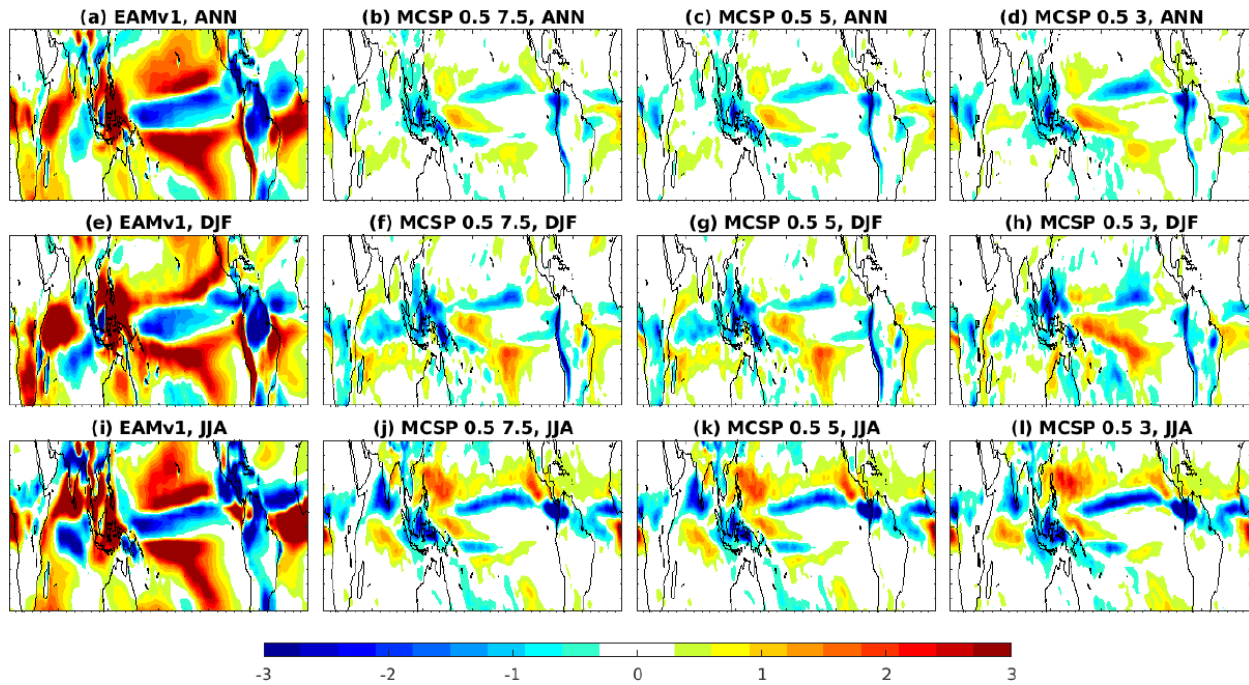
745

746

747

748

749



750

751

752

753

754

755

Figure 15: Similar as Fig. 14 but for E3SMv1 simulations. The first column is the control model simulation biases against GPCP 2.3 and the rest columns are for MCSP with various configurations against the baseline model. The second column is MCSP with $\square = 0.3$, the third column is MCSP with $\square = 0.5$, and the last column is MCSP with $\square = 0.5$ and a zonal wind shear trigger 3 m/s.